Available online at www.sciencedirect.com
SCIENCE DIRECT®
International Journal of Heat and Mass Transfer 47 (2004) 4771–4783
International Journal of HEAT and MASS TRANSFER
www.elsevier.com/locate/ijhmt

# Dynamic bubble behavior during boiling in bead-packed structures

Z. Wang [a], X.F. Peng [b,*], J.M. Ochterbeck [a]

[a] Department of Mechanical Engineering, Clemson University, Clemson, SC 29634, USA
[b] Department of Thermal Engineering, Tsinghua University, Beijing 100084, China

Received 5 December 2003; received in revised form 20 May 2004

**Abstract**

An experimental investigation was conducted to visually observe the boiling behavior in a three-dimensional porous structure made of staggered glass beads, especially the dynamic bubble process and pore-scale liquid flow around bubbles associated with the heat and mass transport taking place at the bubble interface. The experiments show that the dynamic bubble behavior was significantly affected by the bead-packed structure, and several unique boiling phenomena caused by special pore geometry were observed and discussed. The bubble shape and primary bubble interface were described using a force balance acting on the bubble. A theoretical study was performed to describe and evaluate the behavior of the replenished liquid and associated interfacial transport effects. It was concluded from the theoretical analysis that the bubble interface is regulated by interfacial heat and mass transport to provide sufficient driving force for the replenishment. This conclusion is in agreement with the experimental observation.


*Keywords:* Interface; Bubble dynamics; Boiling; Bead-packed structure; Replenishment

## 1. Introduction

Owing to their critical technological applications, much work has been done for fluid flow and heat transfer involving phase-change in porous media in the last two decades [1,2]. In recent years, experimental and theoretical investigations of boiling heat transfer, especially dynamic behaviors of liquid–vapor interfaces in porous structures were performed associated with the development of the porous or capillary-structure evaporators for CPL (capillary pumped loops) and LHP (loop heat pipe) systems [3–8]. As the most important component, a capillary evaporator represents the heart of a CPL system and correspondingly determines the available capillary pumping head for heat transport of the overall loop [3,4]. Depriming and dryout of the capillary structure due to excess heat addition or system transients can result in failure of the entire system without an appropriate rewetting in the porous structure [3,9]. The knowledge of unique interfacial phenomena induced by important geometric configurations in the porous structure is necessary for describing transport processes associated with basic boiling characteristics and improving the pump performance of capillary-driven evaporators [10,11].

* Corresponding author. Tel.: +86 10 6278 9751; fax: +86 10 6278 9751/6277 0209.
*E-mail address:* pxf-dte@mail.tsinghua.edu.cn (X.F. Peng).

0017-9310/$ - see front matter © 2004 Elsevier Ltd. All rights reserved.
doi:10.1016/j.ijheatmasstransfer.2004.05.032

**Nomenclature**

| | |
|---|---|
| $A$ | area [$m^2$] |
| $\overline{A}$ | Hamaker constant [J] |
| $Ca$ | Capillary number [–] |
| $D$ | diameter [m] |
| $F$ | force [N] |
| $g$ | gravitational acceleration [$m^2/s$] |
| $h$ | height [m] |
| $h_e^*$ | dimensionless evaporative heat transfer coefficient [–] |
| $h_{fg}$ | latent heat of liquid–vapor phase-change [kJ/kg] |
| $J$ | Leverett function [–] |
| $k$ | thermal conductivity [W/m K] |
| $K$ | permeability [$m^2$] |
| $K_r$ | relative permeability [–] |
| $L$ | elongation [–] |
| $\dot{m}$ | mass flux [kg/s] |
| $P$ | pressure [Pa] |
| $P_d$ | disjoining pressure [Pa] |
| $q''$ | heat flux [$kW/m^2$] |
| $Q$ | heat input [kW] |
| $r, z$ | coordinates in physical domain [m] |
| $R$ | radius [m] |
| $T$ | temperature [K] |
| $\Delta T^*$ | dimensionless superheat [–] |
| $u$ | velocity [m/s] |
| $V$ | volume [$m^3$] |

*Greek symbols*

| | |
|---|---|
| $\beta$ | vapor fraction [–] |
| $\gamma$ | liquid/vapor kinematic viscosity ratio [–] |
| $\delta$ | thickness [m] |
| $\eta$ | non-dimensional distance [–] |
| $\theta$ | angle [rad] |
| $v$ | kinematic viscosity [$m^2/s$] |
| $\xi$ | coordinates in physical domain [m] |
| $\rho$ | density [$kg/m^3$] |
| $\sigma$ | surface tension [N/m] |
| $\phi$ | porosity [–] |

*Subscripts*

| | |
|---|---|
| 0 | non-evaporating |
| 1, 2, 3 | index in Fig. 6 |
| c | capillary |
| d | detachment |
| e | evaporation |
| eff | effective |
| G | gravity |
| i | interface |
| l | liquid |
| m | meniscus |
| p | solid particle |
| pk | peak value |
| pore | pore |
| r | replenishment |
| shade | shaded part |
| v | vapor |
| w | heated wall |
| $\sigma$ | associated with surface tension |

The contribution of interfacial effects on boiling heat transfer is extremely distinct in porous media, where unique phenomena, or problems, may arise because the dynamic behavior of the bubble interface is significantly affected by the porous structure during boiling [10]. Udell [12] indicated that a heat pipe effect existed in the two-phase zone of porous media, where transport phenomena and fluid flow were similar to conventional heat pipe operation. Based on this understanding, the countercurrent two-phase flow inside the two-phase zone was described and the corresponding dryout limit was predicted. Khrustalev and Faghri [13] investigated heat transfer in an inverted meniscus type evaporator, even at high heat fluxes. The location and shape of the liquid–vapor interface was predicted and critical mechanisms were obtained by solving the problem of an evaporating capillary meniscus at pore-level length scale. The dryout heat flux was discussed in an excellent review by Dhir [2], the dryout being considered as a hydrodynamic process. The focus of this discussion was the influences of the important length scale, or particle sizes, on the dryout limit. In other words, the influence of geometric factors of the porous media on the critical boiling heat transfer characteristics was emphasized in this work. A visual study [14,15] was conducted to understand the phase-change heat transfer in a two-dimensional porous structure heated with a permeable boundary. Using a high-speed video imaging system, both pore-scale bubble dynamic behavior and continuum-scale distribution of the two-phase zone in the porous structure were observed. The important effects of geometric structure on boiling heat transfer were clarified further, although this work did not describe the influence of geometric structure on the dynamic behavior of the bubble interface.

An experimental investigation was conducted in a previous work [11] to visually observe the boiling phenomenon in a three-dimensional porous structure consisting of staggered glass beads. Using a CCD camera, pore-scale interfacial behavior of growing bubbles was explored. The narrowness of the pore structure was

found to significantly affect the nucleation and bubble growth. In the present investigation, more detail observations were conducted further to explore the interfacial phenomena in the bead-packed structure, where issues were addressed regarding the unique bubble behavior and boiling characteristics. Influences of glass beads sizes, applied heat fluxes and working fluid properties on the bubble shape were illustrated. The important influence of liquid replenishment on the bubble dynamic process also was investigated in the bead-packed structure, and a theoretical analysis was performed to describe and evaluate the evaporation-replenishment process.

## 2. Experiments

### 2.1. Experimental apparatus

The experimental apparatus employed in this investigation is shown in Fig. 1. A transparent test section was packed with glass beads, having an average particle diameter of $D_p = 3.5$ or 7 mm. The phase-change behaviors within the bead-packed structure could be observed through the front glass-pane. The bead-packed structure saturated with working fluid was heated from the vessel bottom by a heating assembly consisting of a labyrinth-type foil heater mounted at the bottom and a DC power supply. A Redlake MotionScope-1000s imaging system equipped with zoom capability, with a maximum acquisition-rate of 1000 frames/s, was used to visualize the bubble behavior at the pore level of the bead-packed structure. The view scope of the CCD camera is shown in Fig. 1. Wang et al. [11] described the experimental devices and test procedures in detail. Experiments were performed under different conditions, including various pore structures, fluids, and thermal boundary conditions.

It should be noted that the photographs were taken through a front flat glass-pane of the test section and the phenomena observed occurred in the region adjacent to the glass-pane rather than in the inner regions of the bead-packed structure in the present visual observations. But the geometric structures of these two regions are similar although the effective pore sizes are different. Hence, the information obtained, such as the configuration of bubble interface, dynamic bubble behavior and the interfacial transport processes, can still provide excellent experimental evidence for understanding the phenomena and physical mechanisms.

### 2.2. Dynamic bubbles at pore-level

For subcooled water at the ambient pressure and a temperature of 18.4 °C consecutive snapshots of a typical bubble growth–collapse cycle are presented in Fig. 2 at a moderate heat flux of 36.8 kW/m$^2$. The bubble release frequency was very low due to high subcooling of the ambient liquid. It was observed at the pore-level that bubble sites in the narrow-gap corner (narrow area between a glass bead and the heated surface) were more plentiful than other areas. Small bubbles generated from the narrow-gap corners expanded and penetrated into the main cavities formed by neighboring glass beads, and merged to a larger bubble (or so-called primary bubble) (Fig. 2(b) and (c)). As the primary bubble grew, the pore size became the restriction for further growth of the bubble, and the primary bubble distorted and

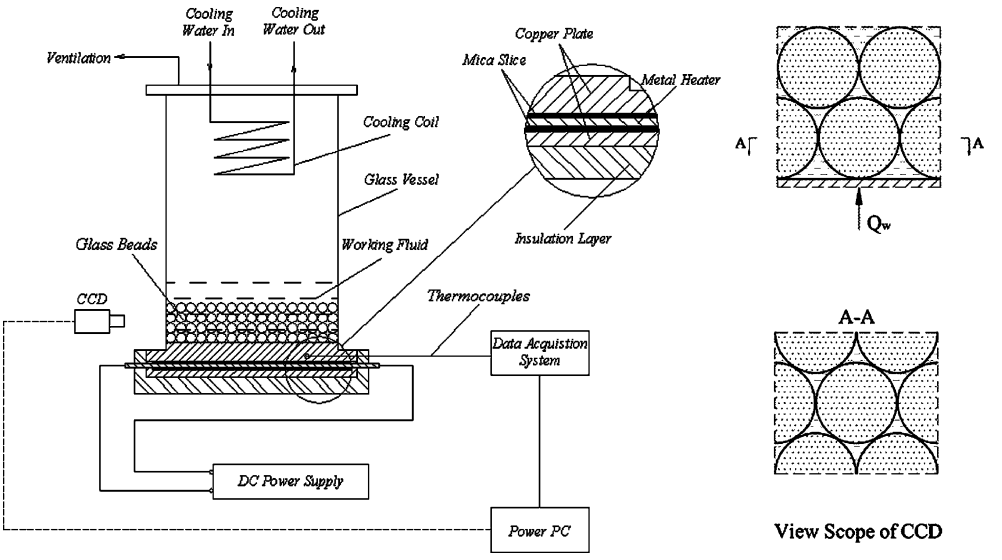


Fig. 1. Experimental apparatus.

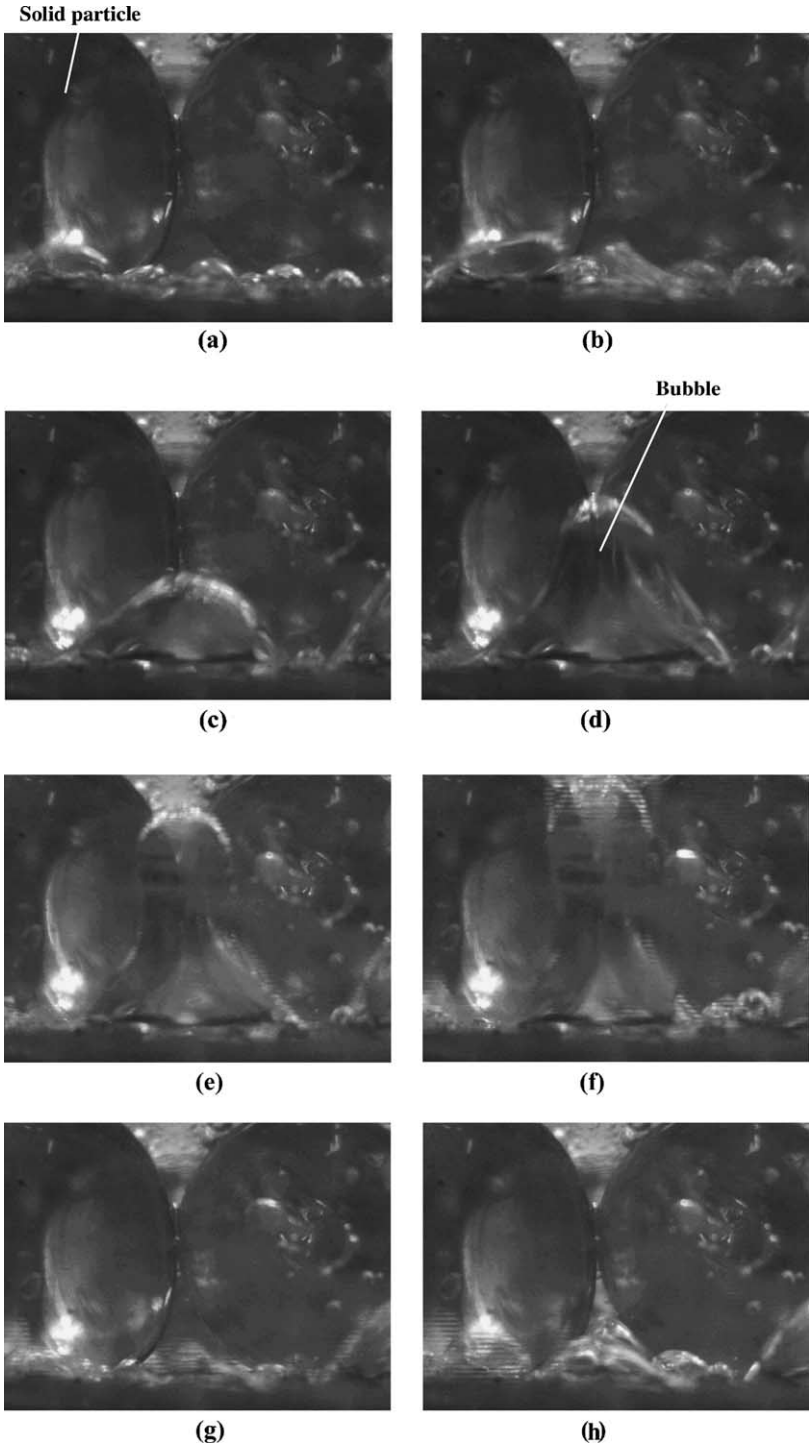


Fig. 2. Bubble behavior in 7 mm bead-packed structure at $q'' = 36.8$ kW/m$^2$ (water). (a) $t = 0.00$ (s), (b) $t = 0.15$ (s), (c) $t = 0.36$ (s), (d) $t = 0.82$ (s), (e) $t = 1.12$ (s), (f) $t = 3.41$ (s), (g) $t = 3.46$ (s) and (h) $t = 3.72$ (s).

elongated (Fig. 2(d) and (e)). Subsequently, the bubble was truncated at the neck of the elongated bubble and quickly escaped from the pore (Fig. 2(f)). Immediately following the primary bubble collapse, the pore space

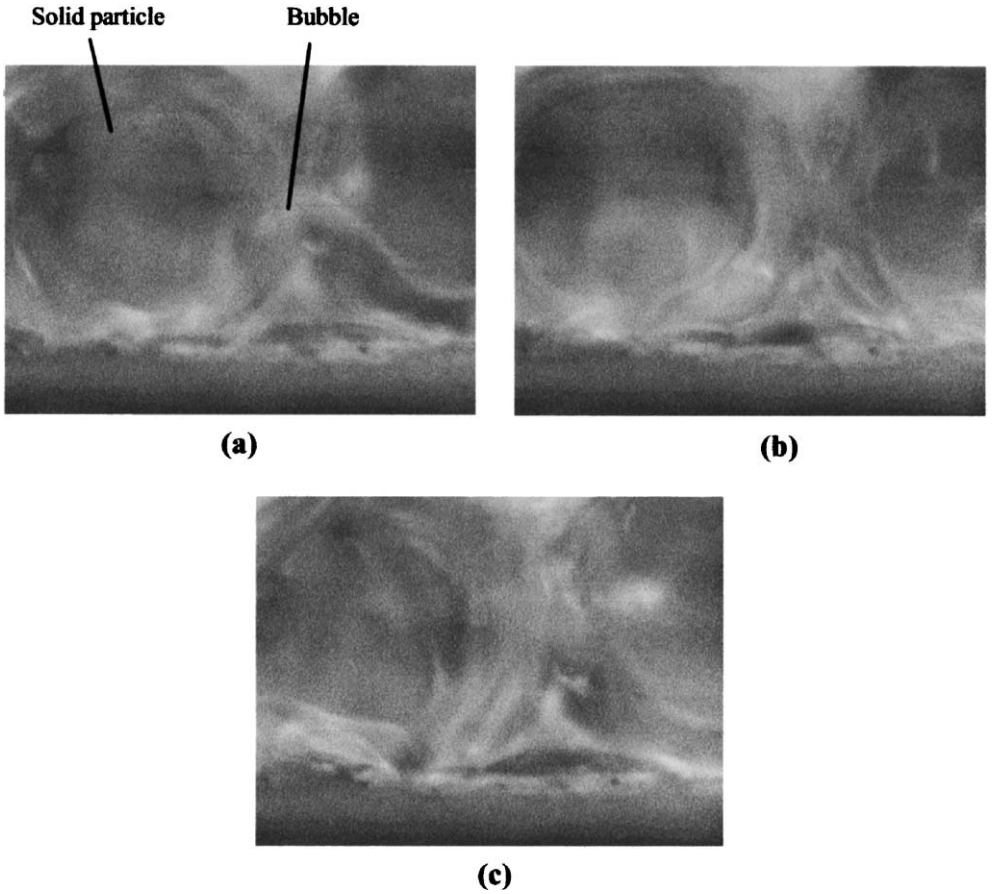


Fig. 3. Bubble behavior in 7 mm bead-packed structure at $q'' = 121.3$ kW/m$^2$ (water). (a) $t = 0.00$ (s), (b) $t = 0.04$ (s) and (c) $t = 0.12$ (s).

was re-occupied by the replenished liquid due to capillary forces (Fig. 2(g)), and another bubble cycle followed (Fig. 2(h)).

As the applied heat flux was increased, approaching the CHF, the scene of pore-scale phase-change behavior was highly disordered, as shown in Fig. 3. Under this condition, primary bubbles coalesced immediately once generated and the heated surface was covered by the vapor phase most of the time during tests. The wall temperature was highly unsteady, and sometimes as high as 200 °C. However, actual dryout of the entire heated surface could not be observed, even at very high heat fluxes, and dryspots on the heated surface were observed to be rather unsteady because of the intensive "evaporation-replenishment" processes in the narrow-gap corners. It was seen from Fig. 3 that the bubble interface expanded horizontally at a high heat flux. In particular, the pore space near the heated surface was vapor-filled except for the liquid menisci in the narrow-gap corners. The vapor front on the heated surface tended to expand into the narrow-gap corner due to evaporation from the liquid meniscus. This variation of the bubble interface profile would resulted in a larger driving force (capillary pressure gradient) for the replenishing-liquid flow. Dry areas on the heated surface were wetted by the subcooled replenishing-liquid. Obviously, this evaporation-replenishment process became more intensive with increasing heat flux, and the narrow-gap corners were highly resistant to dryout even at very high heat fluxes.

## 3. Bubble behavior in bead-packed structure

### 3.1. Pore geometry and boiling process

Peng et al. [10] noted that the dynamic bubble behavior is significantly affected by the bead-packed structure, especially the pore structure adjacent to the heated surface. Generally, the pore structure is divided into three areas [10], as illustrated in Fig. 4(b): the main cavity that is occupied by a primary bubble, the narrow-gap corner zone between a glass bead and the heated surface, and the bridge-channel connecting two neighboring

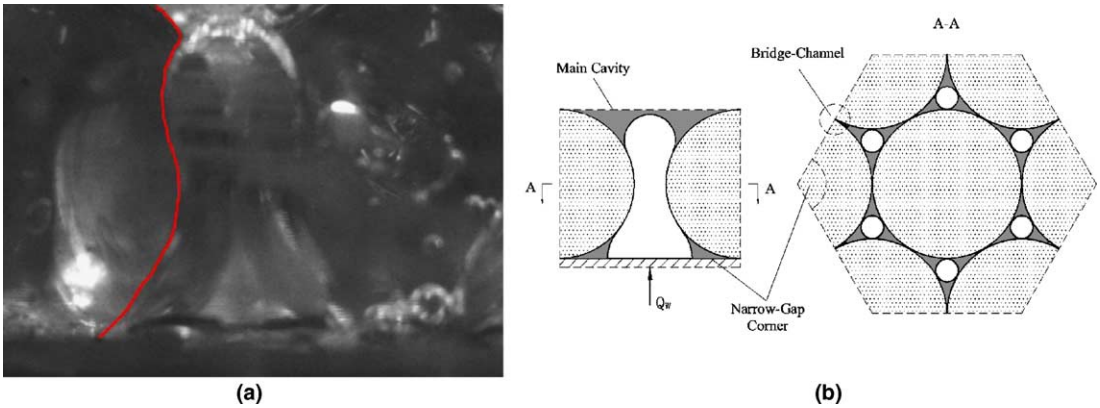


Fig. 4. Pore geometry and bubble interface: (a) a fully developed bubble configuration and (b) pore geometry.

primary bubbles or main cavities. Special pore geometry changes the boiling process, especially the bubble behavior, and thus influences the boiling heat transfer mechanism:

(1) Bubble generation: active sites for boiling on a plain surface randomly distribute on the heated surface, however, bubble sites display regularly depending on pore geometry in the bead-packed structure. Active nucleation sites mainly exist in the narrow-gap corner zone, where most vapor embryos initialize from this area. Small vapor embryos generating from the narrow-gap corners grow up into the main cavity and merge into a primary bubble.

(2) Bubble growth: during the initial stage of bubble growth, the bubble is very small and the pore structure is not a limiting factor for bubble growth. For this inertia-controlled early stage of the bubble growth process, the bubble has nearly a hemispherical shape [16]. With the restriction of pore size exerted on the growing bubble, the bubble grows into a converging–diverging shape and deforms while the vapor front of the growing bubble remains spherical due to surface tension. A typical fully developed bubble is shown in Fig. 4(a). As illustrated in Fig. 4, the pore space near the heated surface is vapor-filled with liquid menisci in the narrow-gap corners. For a fully developed bubble, bubble growth is mainly controlled by the evaporative heat transfer on the liquid meniscus in the narrow-gap corner. The liquid meniscus becomes thinner with increasing heat flux but it does not vanish even at very high heat fluxes. During evaporation on the liquid meniscus, the replenishing-liquid is pulled into the narrow-gap corner by capillary pressure. Owing to the replenishment, the narrow-gap corner zone maintains excellent wetting performance to protect the heated surface from full dryout. Consequently, the boiling heat transfer was enhanced by this evaporation-replenishment process.

(3) Bubble detachment: with the action of buoyancy, the concave section slims down as the bubble elongates gradually. Subsequently, the bubble is truncated at the neck of the elongated bubble and departs rapidly from the pore. This process was favorable for bubble release. In a very short period after bubble detachment, the liquid is sucked into the pore, which accelerates the forthcoming bubble nucleation process and the onset of next bubble cycle.

### 3.2. Static description of primary bubble interface

Based on the observation of bubble dynamics in the bead-packed structure, the profile of primary bubble interface is modeled within the low-heat-flux regime, which is referred to as a static description compared with the dynamic behavior of bubble interface in the high-heat-flux regime. The interface of a fully developed bubble is divided into three parts: I—top section, II—concave section, III—base section, where each part will be described separately. As shown in Fig. 5, the top section interface is a spherical coronal, the base section interface is approximately a part of a hemisphere, and the concave section interface is assumed to touch the solid particle surface directly. Then, the bubble profile can be described by five primary configuration parameters as

$$R_2 = R_p(\sec 30^\circ - 1) \tag{1}$$

$$\tan\theta_1 = (R_2 + R_p)/R_p \tag{2}$$

$$R_3 = (\sec\theta_1 - 1)R_p \tag{3}$$

$$R_1 = (R_2 + R_p)\csc(\pi - \theta_2) - R_p \tag{4}$$

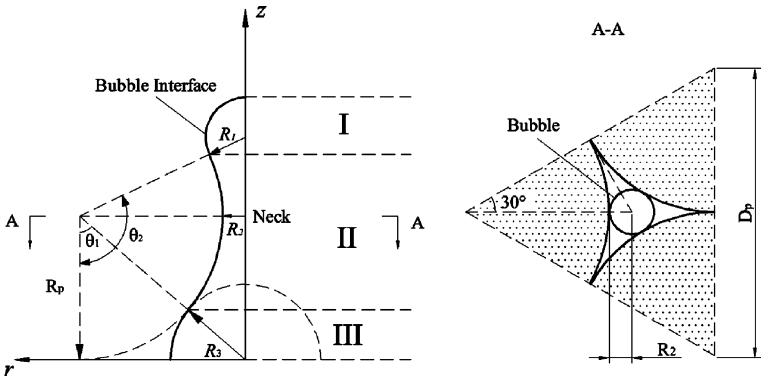


Fig. 5. Bubble interface model.

These four relations indicate that the bubble shape is determined by only one parameter, $\theta_2$, if the particle diameter is specified.

For a fully developed bubble, it can be assumed that only the top section interface moves as the bubble grows (this is not valid at a very high heat flux and will be discussed in the later section). The position of the vapor front at the top is determined by $\theta_2$. For a given working fluid, the departing bubble shape (bubble profile before departing) can be obtained through a force balance between the forces retaining and detaching the bubble. Assuming the inertial effect is negligible during heat-transfer-controlled growth, interfacial tension tends to hold the bubble, while buoyancy acts to draw the bubble away, as shown in Fig. 6, or

$$F_\sigma = F_G \tag{5}$$

Since the bubble is truncated at the neck, the interfacial force, $F_\sigma$, is

$$F_\sigma = 2\pi R_2 \sigma \tag{6}$$

And the buoyancy is expressed as

$$F_G = \rho_l (V_d - V_{shade}) g - \rho_v V_d g + \pi R_2^2 (P_v - P_l)_{shade} \tag{7}$$

where $V_d$ and $V_{shade}$ are given in terms of primary configuration parameters as

$$V_d = \frac{\pi}{3}[R_{1d}(1+\cos(\pi-\theta_{2d}))]^2[3R_{1d} - R_{1d}(1+\cos(\pi-\theta_{2d}))] + \int_{\frac{\pi}{2}}^{\theta_{2d}} \pi[R_p + R_2 - R_p \sin(\pi-\theta)]^2 R_p \sin\theta \, d\theta \tag{8}$$

$$V_{shade} \cong \pi R_2^2 (R_{1d} - (R_{1d} + R_p)\cos\theta_{2d}) \tag{9}$$

The vapor pressure is assumed to be uniform inside the bubble, and the liquid pressure near the top section interface, $P_l$, is obtained from the Young–Laplace equation as

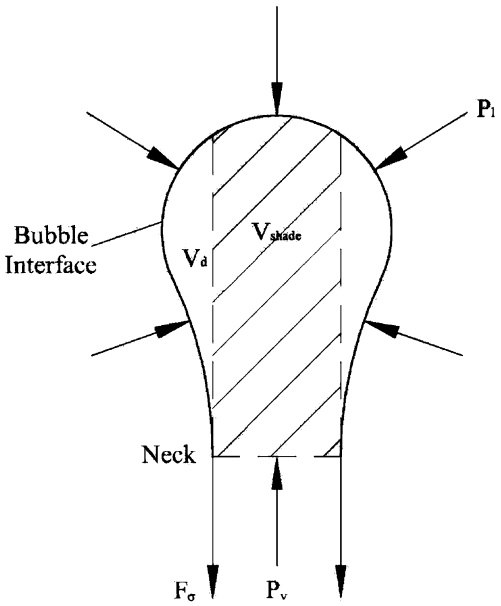


Fig. 6. Forces acting on the bubble above its neck.

$$P_l = P_v - \frac{2\sigma}{R_{1d}} \tag{10}$$

Combining Eqs. (5)–(10), the departing bubble profile corresponding to the departure angle $\theta_{2d}$ is determined by the following equation:

$$\frac{(\rho_l - \rho_v) V_d g - \rho_l V_{shade} g}{2\pi R_2 \sigma} + \frac{R_2}{R_{1d}} = 1 \tag{11}$$

### 3.3. Comparison of results

In Fig. 7, the theoretical prediction of the departing bubble profile is compared with experimental photographs of a growing bubble (Fig. 7(a)) and a departing

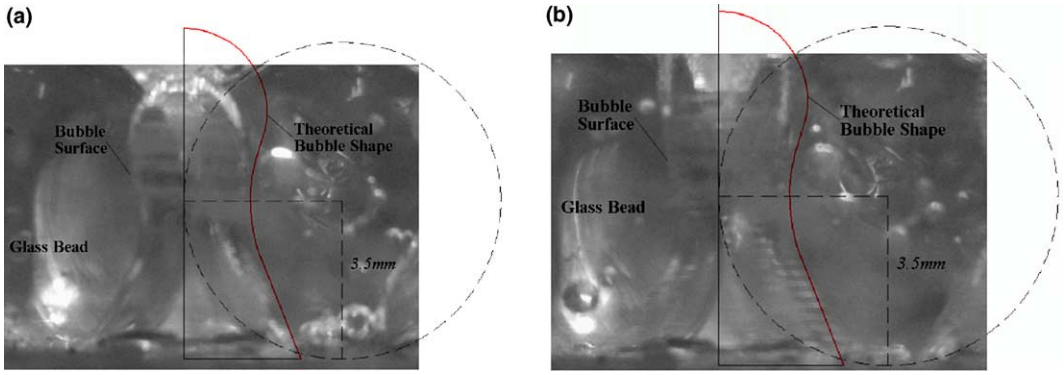


Fig. 7. Comparison of bubble interfaces: (a) growing bubble and (b) departing bubble ($D_p$=7 mm, water).

bubble (Fig. 7(b)). The predicted bubble profile is in good agreement with the real interface of a departing bubble (see Fig. 7(b)). It can be also observed that there is a reasonable consistency between the prediction and the real shape at the bubble interface below the neck for a growing bubble as well as for a departing bubble. This supports the assumption that only the top section interface of a fully developed bubble alters during bubble growth in the low-heat-flux regime.

As shown in Fig. 8, the departure angle, $\theta_{2d}$, and the relative departure diameter, $2R_{1d}/D_p$, of the primary bubble, determined by Eqs. (11) and (4), increases with decreasing particle diameter, as a result of increasing capillary contribution compared with buoyancy. This implies that the narrowness of the pore structure becomes more important for smaller particles. A configuration parameter, bubble elongation $L$, was presented to represent the distortion of the bubble due to the narrowness of pore space

$$L = \frac{h}{D_p} \tag{12}$$

where $h$ is the characteristic height of the primary bubble. For a departing bubble,

$$h_d = \left(\frac{V_d}{V_{pore}} + 0.5\right) D_p \tag{13}$$

where the cavity volume $V_{pore} = D_p^3(\sqrt{3} - \pi/3)/4$. Apparently, bubble elongation represents the narrowness of the pore structure and increases quickly with decreasing particle diameter, as illustrated in Fig. 8(b). Additionally, the departure diameter, $2R_{1d}$, is much larger than the cavity size for very small particles. Under this condition, the pore space already has been fulfilled by the vapor before the bubble detachment. Therefore, smaller particles, and consequently smaller pore space, provides more possibilities for the occurrence of stable dryspots on the heated surface. Further study needs to be performed to

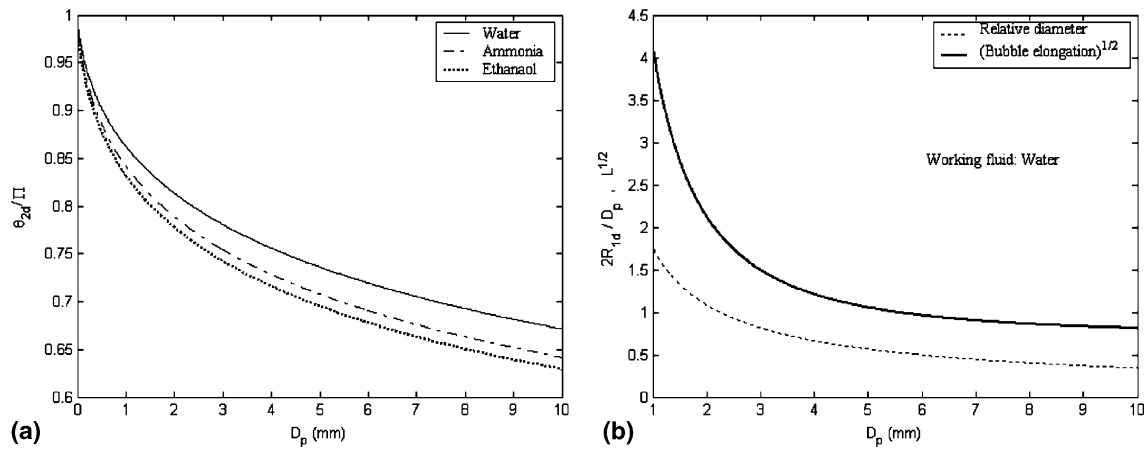


Fig. 8. Departing bubble profile: (a) departure angle vs. particle diameter and (b) relative departure diameter and bubble elongation vs. particle diameter.

understand the bubble detachment mechanism in a porous structure with very small particles.

## 4. Replenishment and dynamic behavior of interface

For boiling in the bead-packed structure, a downward replenishing-liquid flow around the deformed bubble interface is driven by the capillary pressure gradient. Peng et al. [17] indicated that the liquid flow around the bubble is induced virtually by the evaporation and condensation taking place at the bubble interface. The replenishment provides the necessary liquid supply required by evaporation at the bubble interface in the narrow-gap corner area.

### 4.1. Replenishing-liquid flow

As seen in Fig. 9, the curvature of the liquid–vapor interface in the narrow-gap corner zone is usually much larger than that of a bubble interface at other locations. Accordingly, a negative capillary pressure gradient along the $z$-directional coordinate is found. Under the influence of this pressure gradient, the replenishing-liquid flows into the gap corner area.

With a view of the pores in the bead-packed structure as being a system of parallel, equilaterally staggered capillary ducts, a preliminary analysis is conducted to determine driving forces for the pore-scale replenishing-liquid flow using the general concepts of porous media and Darcy's approximation, as shown in Fig. 9. Neglecting gravitational effects, the area-averaged mass flux of liquid (replenishment flux) and vapor (evaporation flux) flow inside the pore can be described as follows:

$$\frac{dP_l}{dz} = \frac{\dot{m}_r v_l}{KK_{rl}} \tag{14}$$

$$\frac{dP_v}{dz} = -\frac{\dot{m}_e v_v}{KK_{rv}} \tag{15}$$

where the permeability of the porous structure $K = D_p^2\phi^3/150(1-\phi)^2$, and relative permeabilities of liquid and vapor phases are represented as [18]

$$K_{rl} = (1-\beta)^3 \tag{16}$$

$$K_{rv} = \beta^3 \tag{17}$$

with $\beta$ being the vapor fraction in the pore. Subtracting Eq. (14) from Eq. (15) and noting that the evaporation flux is balanced by the replenishment flux, i.e. $\dot{m}_r = \dot{m}_e$, results in the capillary pressure gradient

$$\frac{dP_c}{dz} = -\frac{\dot{m}_r}{K}\left(\frac{v_v}{K_{rv}} + \frac{v_l}{K_{rl}}\right) \tag{18}$$

Eq. (18) is given in dimensionless form as

$$\frac{dJ(\beta)}{d\eta} = -Ca\left(\frac{1}{K_{rv}} + \frac{\gamma}{K_{rl}}\right) \tag{19}$$

where

$$J(\beta) = \frac{P_c(\beta)}{\sigma}\sqrt{\frac{K}{\phi}}, \qquad \eta = \frac{z}{\sqrt{K\phi}},$$

$$\gamma = \frac{v_l}{v_v}, \qquad \text{and} \qquad Ca = \frac{\dot{m}_r v_v}{\sigma} = \frac{\dot{m}_e v_v}{\sigma}$$

The Leverett function [19], $J(\beta)$, was correlated by Udell [12] as

$$J(\beta) = 1.417\beta - 2.120\beta^2 + 1.263\beta^3 \tag{20}$$

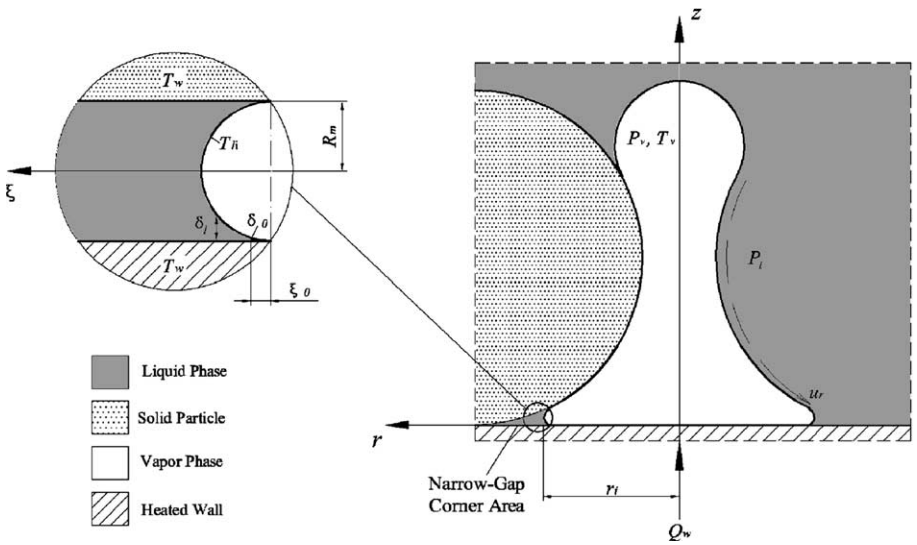


Fig. 9. Replenishment and interface.

which is a function only of $\beta$, or

$$\frac{dJ(\beta)}{d\eta} = \frac{dJ(\beta)}{d\beta}\frac{d\beta}{d\eta} \tag{21}$$

Thus, the differential equation becomes

$$\frac{d\beta}{d\eta} = -\frac{Ca\left(\frac{1}{K_{rv}} + \frac{\gamma}{K_{rl}}\right)}{J'} \tag{22}$$

An equation similar to Eq. (22) also were obtained by Udell [12]. The appropriate boundary condition of Eq. (22) at the bubble top is

$$\beta = 0 \quad \text{at } \eta = \frac{h_d}{\sqrt{K\phi}} \tag{23}$$

Eq. (22) can be integrated numerically to obtain the vapor fraction profile in the pore, or a dynamic description of the bubble interface.

### 4.2. Dynamic behavior of bubble interface

At a high heat flux, the bubble interface profile, especially the interface in the narrow-gap corner, does vary with the applied heat flux. To balance the replenishment flux and the evaporation flux, the bubble interface is regulated by the evaporative heat transfer to establish an appropriate capillary pressure gradient for the replenishing-liquid flow. As illustrated in Figs. 10 and 11, the vapor fraction increases continuously from the top of the bubble to the heated surface; and correspondingly, a negative capillary pressure gradient, driving a downward replenishing-liquid flow, exists along the $\eta$-directional coordinate. Fig. 10 also shows that the vapor fraction profile (or the bubble interface profile) varies with the Capillary number, *Ca*. As the *Ca* increases, the vapor fraction enlarges; that is, the bubble interface expands horizontally, which is in agreement with the experimental observation shown in Fig. 3. Consequently, a larger capillary pressure gradient is established for a higher *Ca* in order to keep the mass balance between the replenishment and the evaporation, as seen in Fig. 11.

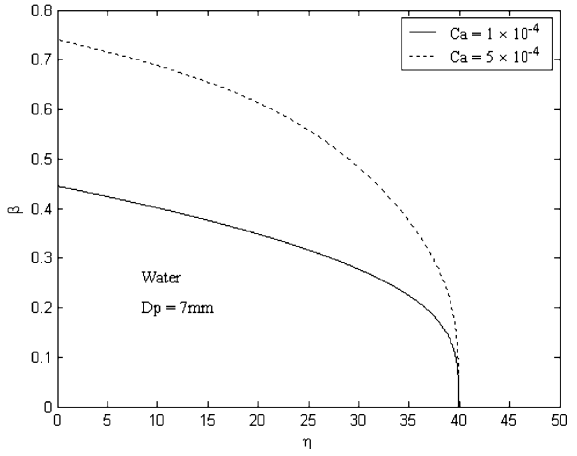


Fig. 10. Vapor fraction profiles.

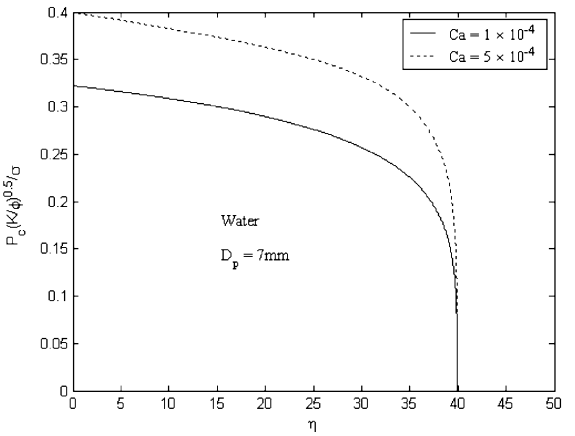


Fig. 11. Capillary pressure profiles.

The bubble interface, especially the interface adjacent to the heated surface, tends to expand horizontally with increasing applied heat flux. The relation between the vapor fraction on the heated surface, $\beta_w$, and the Capillary number is illustrated in Fig. 12. The variation of $\beta_w$ allows a qualitative description of the geometry of the liquid–vapor interface adjacent to the heated surface (Fig. 13). As illustrated in Fig. 13, the liquid–vapor interface expands into the narrow-gap corner area with increasing applied heat flux, and the effective meniscus radius continuously reduces as the liquid meniscus becomes thinner. As a result, the capillary pressure driving the replenishing-liquid flow increases with increasing

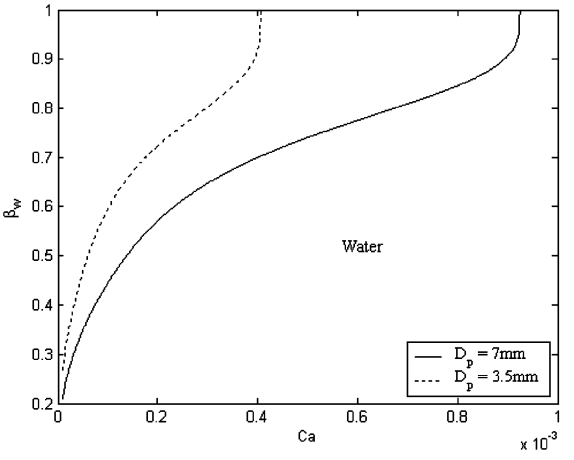


Fig. 12. Vapor fraction on the heated surface vs. Capillary number.

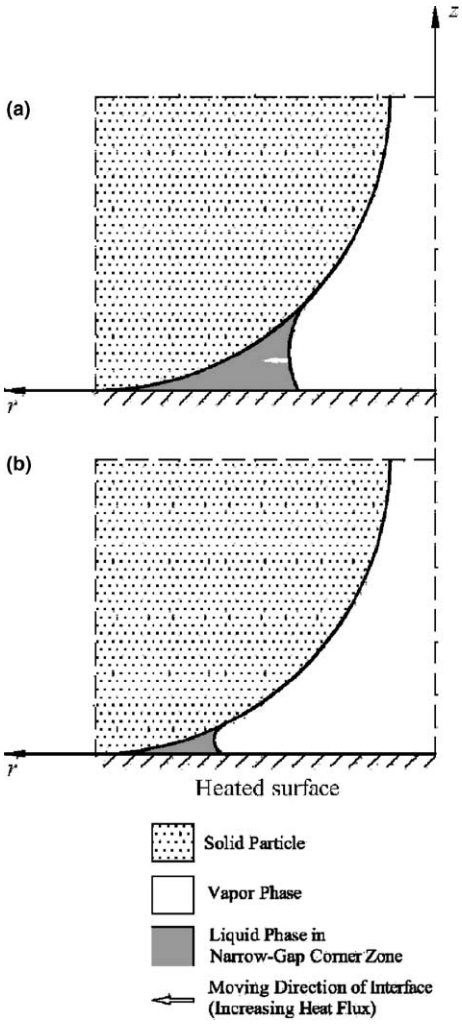


Fig. 13. Liquid–vapor interface adjacent to the heated surface: (a) low heat flux and (b) high heat flux.

heat flux. In conclusion, the bubble interface is regulated by interfacial heat and mass transport to provide sufficient driving force for the replenishment. This also is consistent with the observed experimental evidence (see Fig. 3).

### 4.3. Interfacial heat and mass transfer at pore-level

The replenishment is highly involved with the interface and induced by the interfacial heat and mass transport. The boiling heat transfer is improved by this "evaporation-replenishment" mode in the bead-packed structure. Following the analysis of Chien and Webb [20], the pore-scale interfacial heat transfer can be idealized as a problem of evaporation on the liquid meniscus in the narrow-gap corner by assuming that the evaporation mainly takes place at the bubble interface within the narrow-gap corner zone, as shown in Fig. 9. Other important assumptions are introduced as

(1) The temperatures of both the heated wall and solid particle surface in the gap corner are constant, $T_w$.
(2) The vapor phase inside the bubble is saturated.
(3) The curvature of the liquid meniscus varies with the applied heat flux, but independent of $\xi$ for very small meniscus in the narrow-gap corner. Therefore, the radius of the liquid meniscus, $R_m$, can be expressed as (see Fig. 9)

$$R_m = \frac{1}{2}\left[R_p - \sqrt{R_p^2 - (R_p + R_2 - r_i)^2}\right] \tag{24}$$

(4) The temperature distribution is linear within the thin liquid film.

Assumption (4) implies a one-dimensional heat conduction across the liquid film and gives

$$q_l''(\xi) = k_l \frac{T_w - T_{li}}{\delta_l} \tag{25}$$

where the liquid film thickness, $\delta_l$, can be geometrically obtained from Fig. 9 as

$$\delta_l = R_m - \sqrt{R_m^2 - \xi^2} \tag{26}$$

In Eq. (25), $T_{li}$ is the local liquid temperature at the liquid–vapor interface. Accounting for the effect of capillary pressure and disjoining pressure on the liquid meniscus, Chien and Webb [20] approximately evaluated $T_{li}$ as

$$T_{li} = T_v\left(1 + \frac{P_c - P_d}{\rho_l h_{fg}}\right) \tag{27}$$

where the disjoining pressure $P_d$ is given by [21]

$$P_d = -\frac{\overline{A}}{\delta_l^3} \tag{28}$$

and the Hamaker constant $\overline{A} = 3.11 \times 10^{-21}$ J for water–glass system [22]. Eqs. (25) and (27) can be combined to eliminate $T_{li}$ in favor of $T_w$

$$q_l''(\xi) = k_l T_v \frac{\Delta T_w^* - \left(\frac{P_c - P_d}{\rho_l h_{fg}}\right)}{\delta_l} \tag{29}$$

where $\Delta T_w^* = (T_w - T_v)/T_v$. The total heat rate through a single pore can be evaluated as

$$Q_{pore} = 2\pi r_i \left[2\int_{\xi_0}^{R_m} q_l''(\xi)\,d\xi\right] = \dot{m}_r h_{fg} A_{pore} \tag{30}$$

where $A_{pore} = \sqrt{3}D_p^2/4$. Assuming the meniscus is axisymmetrical, the location of the liquid–vapor interface on the heated surface, $r_i$, is related to the vapor fraction on the heated surface, $\beta_w$, by the following equation:

$$r_i = \sqrt{\frac{\beta_w A_{pore}}{\pi}} \tag{31}$$

The length of liquid film along the coordinate, $\xi_0$, corresponds to the thickness of an equilibrium non-evaporating liquid film, $\delta_0$, or

$$\xi_0 = \sqrt{R_m^2 - (R_m - \delta_0)^2} \tag{32}$$

where $\delta_0$ is the film thickness at which no more evaporation takes place. The equilibrium non-evaporating thickness is expressed as [21]

$$\delta_0 \cong \left[\frac{\overline{A}}{\rho_l h_{fg} \Delta T_w^*}\right]^{1/3} \tag{33}$$

Substituting Eq. (29) into Eq. (30) and rearranging gives

$$Ca = \frac{4 v_v k_l T_v}{\sigma h_{fg}} \sqrt{\frac{\pi \beta_w}{A_{pore}}} \int_{\xi_0}^{R_m} \frac{\left[\Delta T_w^* - \left(\frac{P_c - P_d}{\rho_l h_{fg}}\right)\right]}{R_m - \sqrt{R_m^2 - \xi^2}} \, d\xi \tag{34}$$

Finally, the dimensionless evaporative heat transfer coefficient is defined as

$$h_e^* = \frac{Ca}{\Delta T_w^*} \tag{35}$$

Basing on the equations outlined above, the procedures for predicting the evaporative heat transfer coefficient are summarized here. For a given Capillary number (applied heat load), $\beta_w$ can be determined by Eq. (22) at $\eta = 0$. Then, the geometric parameters of the capillary meniscus can be determined from Eqs. (24), (26) and (31). Afterwards, $\Delta T_w^*$ is obtained by solving Eqs. (32) and (34) simultaneously. The dimensionless evaporative heat transfer coefficient, $h_e^*$, is finally calculated from Eq. (35).

The dimensionless evaporative heat transfer coefficient, $h_e^*$, was predicted as a function of the Capillary number, as shown in Fig. 14. With an increase of the $Ca$ (or applied heat flux), $h_e^*$ gradually increases, reaches a peak value (corresponding to $Ca_{pk}$), and drops rapidly afterwards. The increase of $h_e^*$ during early stages of boiling ($Ca < Ca_{pk}$) may be partly attributed to the fact that the evaporating liquid film in the narrow-gap corner area becomes thinner. Additionally, heat transfer is enhanced also by the violent, repeated dryout–rewetting process observed around the gap corner, which results from unceasing interactions between the replenishment and interfacial evaporation. This dynamic process can accelerate the collapse of dry areas covering the heated surface, and accordingly intensify the fluid mixing. As the imposed heat flux increases further ($Ca > Ca_{pk}$), most area of the heated surface is covered by vapor (see Fig. 12), $h_e^*$ begins to drop due to the loss of evaporating regions. Under this condition, the gap corner area may be surrounded by the vapor phase and the path for the replenishing-liquid flow into the gap corner may be disconnected. Owing to the lack of liquid supply, the advancement and widespread areas of dryout may follow. If this trend continues, dryout of the heated surface may occur. As seen from Fig. 14, higher heat transfer coefficients are exhibited for smaller pore sizes compared to larger pore sizes. This is due to the process of liquid replenishment being significantly intensified in smaller pore structures due to existing, strong capillary effects. But it can be also found that the $Ca_{pk}$ of a 3.5 mm pore structure is much lower than that of a 7 mm pore structure. As mentioned previously, the problem of spatial limitation becomes more serious with decreasing pore size. Due to the extreme narrowness of the pore space, the vapor fraction on the heated surface increases rapidly with heat flux for smaller pore structure (see Fig. 12). Thus, dryout usually occurs much earlier in smaller pore structures.

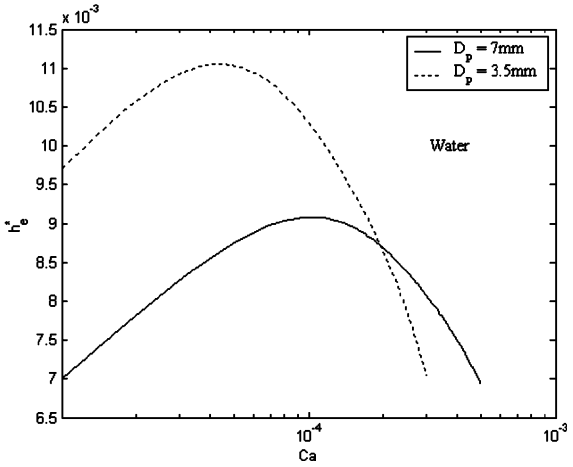


Fig. 14. Dimensionless evaporative heat transfer coefficient vs. Capillary number.

## 5. Conclusions

Boiling characteristics associated with bead-packed structures were experimentally observed and analytically discussed. A theoretical analysis was performed to illustrate how these unique boiling characteristics influence the bubble interfacial behavior.

1. Dynamic bubble behavior is significantly affected by the bead-packed structure. Special boiling phenomena were observed and discussed in accordance with such concepts as narrow-gap corner zone, deformed bubble interface, and evaporation-replenishment process. The boiling characteristics are the consequence of limited bubble growth space. Therefore, the pore structure plays a very important role on the interfacial heat and mass transfer in bead-packed structures.

2. With the consideration of a force balance exerting on the primary bubble, an analytical method was introduced to predict the bubble shape and interface profile. The prediction was reasonably consistence with experimental photographs and comparisons of results indicate that the spatial limitation of pore structure becomes more obvious for smaller particles.
3. As a sequence of the deformed bubble interface, replenishment mainly driven by capillary forces is a unique characteristic in the bead-packed structure affecting the dynamic bubble process. A theoretical study on the behavior of the replenished liquid and associated interfacial transport effects was performed to describe and evaluate the interfacial heat and mass transfer. The analysis shows that the replenishment is highly involved with the interface and interacts with interfacial evaporation. The bubble interface is regulated by this interaction to provide sufficient driving force for liquid replenishment. Under the influence of the evaporation-replenishment process, boiling heat transfer in the pore structure is greatly enhanced.

## Acknowledgment

This work was supported by the National Natural Science Foundation of China (contract nos. 59625612 and 59976016).

## References

[1] C.Y. Wang, P. Cheng, Multiphase flow and heat transfer in porous media, in: J.P. Hartnet, T.F. Irvine, Y.I. Cho, G.A. Greene (Eds.), Advances in heat transfer, vol. 30, Academic Press, New York, 1997, pp. 93–196.
[2] V.K. Dhir, Heat transfer from heat-generating pools and particulate beds, in: J.P. Hartnet, T.F. Irvine, Y.I. Cho, G.A. Greene (Eds.), Advances in heat transfer, vol. 29, Academic Press, New York, 1997, pp. 1–57.
[3] J.M. Ochterbeck, Heat pipes, in: A. Bejan, A. Kraus (Eds.), Handbook of heat transfer, John Wiley & Sons, New York, 2003, pp. 1181–1230.
[4] Yu.F. Maidanik, State-of-the-art of CPL and LHP technology, in: Heat Pipe Science and Technology, Proceedings of 11th International Heat Pipe Conference, Tokyo, 1999, pp. 19–30.
[5] G.P. Peterson, An introduction to heat pipes: modeling, testing and applications, John Wiley and Sons, New York, 1994.
[6] A. Faghri, Heat pipe science and technology, Taylor & Francis, Washington, DC, 1995.
[7] A.S. Demidov, E.S. Yatsenko, Investigation of heat and mass transfer in the evaporation zone of heat pipe operating by the 'inverted meniscus' principle, Int. J. Heat Mass Transfer 37 (14) (1994) 2155–2163.
[8] Y.D. Cao, A. Faghri, Analytical solutions of flow and heat transfer in a porous structure with partial heating and evaporation on the upper surface, Int. J. Heat Mass Transfer 37 (10) (1994) 1525–1533.
[9] X.F. Peng, B.X. Wang, Rewetting of hot surfaces induced by capillary flow, Prog. Nat. Sci. 6 (3) (1996) 333–345.
[10] X.F. Peng, Z. Wang, D.J. Lee, Dynamic behavior of bubble interface during boiling, J. Thermal Sci. 11 (4) (2002) 308–319.
[11] Z. Wang, X.F. Peng, T. Liu, Visualization of boiling phenomena in a bead-packed structure, Exp. Heat Transfer 15 (3) (2002) 177–189.
[12] K.S. Udell, Heat transfer in porous media heated from above with evaporation, condensation, and capillary effects, J. Heat Transfer 105 (2) (1983) 485–492.
[13] D. Khrustalev, A. Faghri, Heat transfer in the inverted meniscus type evaporator at high heat fluxes, Int. J. Heat Mass Transfer 38 (16) (1995) 3091–3101.
[14] Q. Liao, T.S. Zhao, A visual study of phase-change heat transfer in a two-dimensional porous structure with a partial heating boundary, Int. J. Heat Mass Transfer 43 (7) (2000) 1089–1102.
[15] T.S. Zhao, Q. Liao, On capillary-driven flow and phase-change heat transfer in a porous structure heated by a finned surface: measurements and modeling, Int. J. Heat Mass Transfer 43 (7) (2000) 1141–1155.
[16] V.P. Carey, Liquid–vapor phase change phenomena, Hemisphere Publishing, Washington DC, 1992.
[17] X.F. Peng, B.X. Wang, D.M. Christopher, Some fundamentals of boiling in microgravity, in: Heat Transfer Science and Technology 2000—Fifth International Symposium on Heat Transfer, High Education Press, Beijing, 2000, pp. 60–76.
[18] I. Fatt, W.A. Klikoff, Effect of fractional wettability on multiphase flow through porous media, AIME Trans. 216 (1959) 246, AIME technical note no. 2043.
[19] M.C. Leverett, Capillary behavior in porous solids, AIME Trans. 142 (1941) 152–169.
[20] L.H. Chien, R.L. Webb, A nucleate boiling model for structured enhanced surfaces, Int. J. Heat Mass Transfer 41 (14) (1997) 2183–2195.
[21] P.C. Wayner Jr., Y.K. Kao, L.V. Lacroix, The interline heat transfer coefficient of an evaporating wetting film, Int. J. Heat Mass Transfer 19 (5) (1976) 487–492.
[22] J. Gregory, The calculation of Hamaker constants, Adv. Colloid Interface Sci. 2 (1969) 396–417.